*J. Fluid Mech.* (2000), *vol.* 409, *pp.* 121–147. Printed in the United Kingdom



# Numerical simulation of crossing-shock-wave/turbulent-boundary-layer interaction using a two-equation model of turbulence

By D. KNIGHT[1], M. GNEDIN[1], R. BECHT[1] AND A. ZHELTOVODOV[2]

[1]Department of Mechanical and Aerospace Engineering, Rutgers – The State University of New Jersey, New Brunswick, NJ 08903

[2]Institute of Theoretical and Applied Mechanics, Novosibirsk 630090, Russia

(Received 2 January 1999 and in revised form 20 May 1999)

A crossing-shock-wave/turbulent-boundary-layer interaction is investigated using the $k$–$\epsilon$ turbulence model with a new low-Reynolds-number model based on the approach of Saffman (1970) and Speziale *et al.* (1990). The crossing shocks are generated by two wedge-shaped fins with wedge angles $\alpha_1$ and $\alpha_2$ attached normal to a flat plate on which an equilibrium supersonic turbulent boundary layer has developed. Two configurations, corresponding to the experiments of Zheltovodov *et al.* (1994, 1998*a*, *b*), are considered. The free-stream Mach number is 3.9, and the fin angles are $(\alpha_1, \alpha_2) = (7°, 7°)$ and $(7°, 11°)$. The computed surface pressure displays very good agreement with experiment. The computed surface skin friction lines are in close agreement with experiment for the initial separation, and are in qualitative agreement within the crossing shock interaction region. The computed heat transfer is in good agreement with experiment for the $(\alpha_1, \alpha_2) = (7°, 7°)$ configuration. For the $(\alpha_1, \alpha_2) = (7°, 11°)$ configuration, the heat transfer is significantly overpredicted within the three-dimensional interaction. The adiabatic wall temperature is accurately predicted for both configurations.

## 1. Introduction

Three-dimensional shock-wave/turbulent-boundary-layer interactions commonly occur in a wide range of applications in high-speed flows and strongly influence the flow-field characteristics (Greene 1970; Settles & Dolling 1986, 1990; Zheltovodov 1996). For sufficiently strong shocks, the flow pattern includes separation of the boundary layer and formation of vortices. An adequate understanding of the flow structures caused by shock-wave/turbulent-boundary-layer interaction, and the ability of a theoretical model to accurately predict the aerothermodynamic loads (i.e. surface pressure, skin friction and heat transfer), are crucial for the improved design of supersonic aircraft components such as inlets or nozzles.

Recent research efforts have concentrated on a particular family of flows involving three-dimensional shock-wave/turbulent-boundary-layer interactions, namely the crossing shock (‘double fin’) interactions (figure 1), due to applications to high-speed inlets (Edwards 1976; Sakell, Knight & Zheltovodov 1994). Significant research efforts

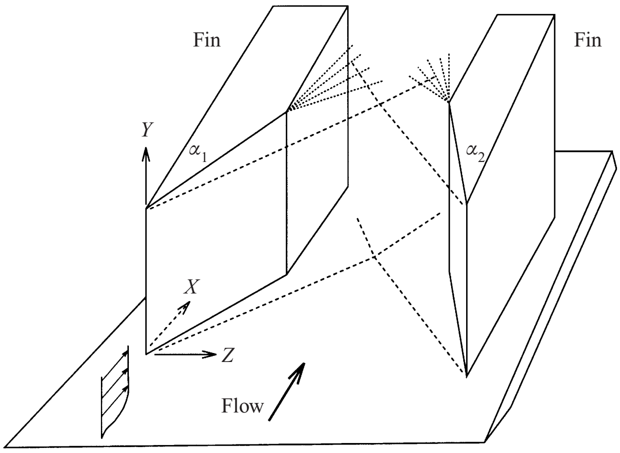


FIGURE 1. Crossing shock ('double fin').

have been concentrated on the development and evaluation of turbulence models capable of providing accurate predictions of the flow structure and aerothermodynamic loads on the bottom flat-plate surface (Narayanswami *et al.* 1992; Narayanswami, Horstman & Knight 1993*a*; Narayanswami, Knight & Horstman 1993*c*); Garrison *et al.* 1992; Garrison & Settles 1992, 1993; Garrison 1994; Garrison *et al.* 1994; Gaitonde, Shang & Visbal 1995; Gaitonde & Shang 1995; Knight *et al.* 1995*a*; Gaitonde *et al.* 1997, 1998). A review of theoretical and experimental studies of the crossing-shock interactions can be found in Knight *et al.* (1995*b*), Degrez (1993), Zheltovodov, Maksimov & Shevchenko (1998*a*) and Zheltovodov *et al.* (1998*b*). The computed flows generally exhibit good agreement with experimental data for surface pressure, shock structure, and boundary layer profiles of pitot pressure and yaw angle. However, the accurate prediction of the surface heat transfer and skin friction remains a challenging problem (Narayanswami *et al.* 1993*a*; Garrison *et al.* 1994).

While the surface pressure is to a large extent determined by the inviscid rotational character of the flow and therefore not strongly affected by the particular choice of the theoretical turbulence model (Knight *et al.* 1995*b*), the surface derivative quantities (i.e. skin friction and heat transfer) are strongly influenced by the turbulence model. Consequently, one of the greatest challenges for accurately computing the crossing shock interaction is the modelling of the turbulence quantities of such flows. The two-equation $k$–$\epsilon$ model is a popular choice since it can in principle predict complex flow fields better than algebraic models and is significantly simpler than sophisticated higher-order closures. A major difficulty in the implementation of the $k$–$\epsilon$ model is the treatment of the near-wall region, where the classical high Reynolds number $k$–$\epsilon$ model is invalid. To overcome this difficulty and allow integration to the boundary, wall damping functions can be introduced which lead to the creation of a so-called 'low-Reynolds-number $k$–$\epsilon$ model'. Many such models have been developed in recent years and significant research efforts have been invested in the validation of different turbulence models for the computation of flows with shock-wave/boundary-layer interaction, in particular flows with crossing shock interactions. In this paper, we present results using the $k$–$\epsilon$ model with the new low Reynolds number model of Becht & Knight (1995) which was developed on the basis of three principles, namely (i) the model employs the physical dissipation rate $\epsilon$, (ii) the normal distance $n$ is avoided, and (iii) the minimum number of modifications is introduced, as described by Speziale, Abid & Anderson (1990). The low Reynolds number modifications, based on the ideas of Saffman (1970) and Speziale *et al.* (1990), are (i) incorporation of molecular diffusion of $k$ and $\epsilon$, (ii) modification of the turbulent eddy viscosity $\mu_T$ to provide proper asymptotic behaviour near the wall, and (iii) modification of the dissipation of $\epsilon$ to avoid singularities in the $\epsilon$ equation near the wall.

The objective of the present paper is to assess the capability of the standard $k$–$\epsilon$ model with the new low Reynolds number model to predict crossing-shock-wave/turbulent-boundary-layer interactions. The experimental configuration of Zheltovodov *et al.* (1994) is considered. Complete details of the experiment are provided in Zheltovodov *et al.* (1998*a, b*). Computational results are compared to the experimental data at $M_\infty = 3.9$ for $(\alpha_1, \alpha_2) = (7°, 7°)$ and $(7°, 11°)$. Comparison is also presented with previous computational results of Knight *et al.* (1995*b*) using the $k$–$\epsilon$ Chien model, and Zha & Knight (1996) using a full Reynolds stress equation model for the $(\alpha_1, \alpha_2) = (7°, 11°)$ case.

## 2. Governing equations

### 2.1. *Reynolds-averaged Navier–Stokes*

The Reynolds-averaged equations for conservation of mass, momentum and energy are

$$\frac{\partial \bar{\rho}}{\partial t} + \frac{\partial \bar{\rho}\tilde{u}_i}{\partial x_i} = 0, \tag{2.1}$$

$$\frac{\partial \bar{\rho}\tilde{u}_i}{\partial t} + \frac{\partial \bar{\rho}\tilde{u}_i\tilde{u}_j}{\partial x_j} = -\frac{\partial \bar{p}}{\partial x_i} + \frac{\partial \mathscr{T}_{ij}}{\partial x_j}, \tag{2.2}$$

$$\frac{\partial \bar{\rho}\tilde{e}}{\partial t} + \frac{\partial (\bar{\rho}\tilde{e} + \bar{p})\tilde{u}_i}{\partial x_i} = \frac{\partial}{\partial x_i}\left(\mathscr{Q}_i + \mathscr{T}_{ij}\tilde{u}_j\right), \tag{2.3}$$

where the Einstein summation convention is employed and the overbar represents ensemble averaging, i.e.

$$\bar{f} = \lim_{n\to\infty} \frac{1}{n}\sum_{v=1}^{v=n} f^{(v)} \tag{2.4}$$

where $f^{(v)}$ are the individual realizations of the variable $f(x, y, z, t)$. A mass-averaged (Favre-averaged) variable $\tilde{f}$ is defined as the density-weighted ensemble average,

$$\tilde{f} = \frac{1}{\bar{\rho}} \lim_{n\to\infty} \frac{1}{n}\sum_{v=1}^{v=n} (\rho f)^{(v)} \tag{2.5}$$

and the fluctuating variable $f''$ in the mass-averaged expansion is

$$f'' = f - \tilde{f}. \tag{2.6}$$

Alternatively, the fluctuating variable $f'$ in the unweighted expansion is

$$f' = f - \bar{f}. \tag{2.7}$$

In (2.1) to (2.3), $\bar{\rho}$ is the mean density, $\tilde{u}_i$ is the mass-averaged velocity, $\bar{p}$ is the mean pressure, and $\tilde{e}$ is the mass-averaged total energy per unit mass,

$$\tilde{e} = c_v\tilde{T} + \tfrac{1}{2}\tilde{u}_i\tilde{u}_i + \tilde{k} \tag{2.8}$$

where $\tilde{k}$ is the mass-averaged turbulence kinetic energy

$$\bar{\rho}\tilde{k} = \tfrac{1}{2}\overline{\rho u_i'' u_i''}. \tag{2.9}$$

The total stress is defined as

$$\mathscr{T}_{ij} = -\overline{\rho u_i'' u_j''} + \bar{\tau}_{ij} \tag{2.10}$$

where the mean molecular viscous stress $\bar{\tau}_{ij}$ is

$$\bar{\tau}_{ij} = -\tfrac{2}{3}\tilde{\mu}\frac{\partial \tilde{u}_k}{\partial x_k}\delta_{ij} + \tilde{\mu}\left(\frac{\partial \tilde{u}_j}{\partial x_i} + \frac{\partial \tilde{u}_i}{\partial x_j}\right) \tag{2.11}$$

where $\tilde{\mu} \equiv \mu(\tilde{T})$. The total heat flux is

$$\mathscr{Q}_i = -c_p\overline{\rho T'' u_i''} - \bar{q}_i \tag{2.12}$$

where the molecular heat flux is

$$\bar{q}_i = -\frac{c_p\tilde{\mu}}{Pr}\frac{\partial \tilde{T}}{\partial x_i} \tag{2.13}$$

and $Pr$ is the molecular Prandtl number.

The Reynolds-averaged equations (2.1) to (2.3) neglect the triple correlation $\frac{1}{2}\,\overline{\rho u_j'' u_j'' u_i''}$ and velocity–molecular shear correlation $\overline{u_i'' \tau_{ij}}$ which are negligible under practical circumstances (Knight 1993*b*).

### 2.2. *Turbulence model for high Reynolds number*

The closure of the Reynolds-averaged equations (2.1) to (2.3) requires specification of the turbulent stress $-\overline{\rho u_i'' u_j''}$ and turbulent heat flux $-c_p\overline{\rho T'' u_i''}$. We adopt the high Reynolds number form of the two-equation $k$–$\epsilon$ model of Jones & Launder (1972). The equation for the turbulence kinetic energy $\tilde{k}$ is taken to be

$$\frac{\partial \bar{\rho}\tilde{k}}{\partial t} + \frac{\partial \bar{\rho}\tilde{k}\tilde{u}_i}{\partial x_i} = -\overline{\rho u_i'' u_j''}\frac{\partial \tilde{u}_i}{\partial x_j} - \bar{\rho}\tilde{\epsilon} + \frac{\partial}{\partial x_i}\left(\frac{\mu_T}{\bar{\rho}\sigma_k}\frac{\partial \bar{\rho}\tilde{k}}{\partial x_i}\right). \tag{2.14}$$

The equation for the dissipation is

$$\frac{\partial \bar{\rho}\tilde{\epsilon}}{\partial t} + \frac{\partial \bar{\rho}\tilde{u}_i\tilde{\epsilon}}{\partial x_i} = -C_{\epsilon 1}\frac{\tilde{\epsilon}}{\tilde{k}}\overline{\rho u_i'' u_j''}\frac{\partial \tilde{u}_i}{\partial x_j} - C_{\epsilon 2}\bar{\rho}\frac{\tilde{\epsilon}^2}{\tilde{k}} + \frac{\partial}{\partial x_i}\left(\frac{\mu_T}{\sigma_\epsilon}\frac{\partial \tilde{\epsilon}}{\partial x_i}\right). \tag{2.15}$$

The turbulent stresses are

$$-\overline{\rho u_i'' u_j''} = \mu_T\left(\frac{\partial \tilde{u}_i}{\partial x_j} + \frac{\partial \tilde{u}_j}{\partial x_i} - \frac{2}{3}\frac{\partial \tilde{u}_k}{\partial x_k}\delta_{ij}\right) - \tfrac{2}{3}\bar{\rho}\tilde{k}\delta_{ij} \tag{2.16}$$

and the turbulent heat flux is

$$-c_p\overline{\rho T'' u_i''} = c_p\frac{\mu_T}{Pr_t}\frac{\partial \tilde{T}}{\partial x_i} \tag{2.17}$$

where the turbulent eddy viscosity is

$$\mu_T = \bar{\rho}C_\mu\frac{\tilde{k}^2}{\tilde{\epsilon}}. \tag{2.18}$$

The turbulence model constants are based on the standard values (Launder & Sharma 1974; Wilcox 1993) and are presented in table 1. The governing equations (2.14) to (2.18) are applicable only within fully turbulent regions, and consequently

| Constant | Value |
|---|---|
| $C_\mu$ | 0.09 |
| $C_{\epsilon_1}$ | 1.44 |
| $C_{\epsilon_2}$ | 1.92 |
| $Pr_t$ | 0.9 |
| $\sigma_k$ | 1.0 |
| $\sigma_\epsilon$ | 1.3 |

TABLE 1. Standard $k$–$\epsilon$ model constants.

cannot be integrated directly to a solid boundary. The low Reynolds number modifications to allow integration to a solid boundary are presented in the following section.

### 2.3. *Turbulence model for low Reynolds number*

We present the motivation, definition and calibration of the low Reynolds number model.

#### 2.3.1. *Motivation*

The first low Reynolds number modification to the $k$–$\epsilon$ model was developed by Jones & Launder (1972, 1973). The modifications included the formal introduction of molecular diffusion in the $k$ and $\epsilon$ equations, incorporation of a functional dependence of two of the model constants on the turbulence Reynolds number $R_t \equiv \rho k^2/\epsilon\mu$, introduction of a pseudo-dissipation rate $\epsilon' = \epsilon - \epsilon_w$ (where $\epsilon_w$ is the turbulent dissipation rate at the wall) apparently on the basis of numerical considerations, and inclusion of additional source terms in the $k$ and $\epsilon$ equations.

Numerous other low Reynolds number modifications for the $k$–$\epsilon$ model have been proposed including, for example, Launder & Sharma (1974), Hoffman (1975), Reynolds (1976), Hassid & Poreh (1978), Dutoya & Michard (1981), Lam & Bremhorst (1981), Chien (1982), Myong & Kasagi (1990), So, Zhang & Speziale (1991), Yang & Shih (1993), and Fan, Lakshminarayana & Barnett (1993). A detailed examination of the first seven of these was performed by Patel, Rodi & Scheuerer (1985) who concluded that the models of Launder & Sharma, Chien, and Lam & Bremhorst yielded comparable results and are significantly more accurate than the others.

The low Reynolds number $k$–$\epsilon$ models recommended by Patel *et al.*, as well as many subsequent models (e.g. Myong & Kasagi 1990; So *et al.* 1991; Fan *et al.* 1993), are characterized by one or more of the following limitations:

(*a*) *Pseudo-dissipation rate* The pseudo-dissipation rate, introduced by Jones & Launder (1972) for numerical reasons, is unphysical. Its use has been criticized for many years (e.g. Reynolds 1976). Although it might be argued that the use of the pseudo-dissipation rate is fundamentally a philosophical question, nevertheless we maintain that, in the absence of a compelling numerical requirement, it is unnecessary. As described later, we have found no numerical difficulties in using the dissipation rate $\epsilon$ and imposing the physically correct boundary condition for $\epsilon$ at the wall.

(*b*) *Dependence on n* The normal distance $n$, employed in many low Reynolds number modifications in the form of the dimensionless distance $n^+ \equiv nu_*/v_w$ (where $u_* \equiv \sqrt{\tau_w/\rho_w}$ and $\tau_w$ is the (local) wall shear stress) or $R_n \equiv \sqrt{k}n/v$, cannot be uniquely defined in all cases. This occurs even for simple geometries (e.g. in the vicinity of a two-dimensional compression corner, in the neighbourhood of a three-dimensional corner, etc.).

(*c*) *Extensive number of modifications* Speziale *et al.* (1990) demonstrated that a minimum of three functional modifications to the $k$–$\epsilon$ model is required for integration to a solid boundary, namely (i) incorporation of molecular diffusion of $k$ and $\epsilon$ (similar to the suggestion of Saffman 1970), (ii) modification of the turbulent eddy viscosity $\mu_T$ to provide proper asymptotic behaviour near the wall, and (iii) modification of the dissipation of $\epsilon$ to avoid singularities in the $\epsilon$ equation near the wall. Many low Reynolds number modifications employ significantly more than this minimum number. While the choice of the low Reynolds number modifications is not unique and the ultimate value is determined by the ability of the model to predict turbulent flows, nonetheless we consider simplicity of the low Reynolds number modifications to be an important attribute.

The new low Reynolds number model avoids all of these limitations.

2.3.2. *Equations for $\tilde{k}$ and $\tilde{\epsilon}$*

The equation for the turbulence kinetic energy (2.14) is modified in two ways. First, molecular diffusion of $\tilde{k}$ is formally incorporated in the manner proposed by Saffman (1970):

$$\frac{\partial \bar{\rho}\tilde{k}}{\partial t} + \frac{\partial \bar{\rho}\tilde{k}\tilde{u}_i}{\partial x_i} = -\overline{\rho u_i'' u_j''}\frac{\partial \tilde{u}_i}{\partial x_j} - \bar{\rho}\tilde{\epsilon} + \frac{\partial}{\partial x_i}\left(\frac{\mu_T}{\bar{\rho}\sigma_k}\frac{\partial \bar{\rho}\tilde{k}}{\partial x_i} + \tilde{\mu}\frac{\partial \tilde{k}}{\partial x_i}\right). \tag{2.19}$$

Second, the turbulent eddy viscosity is modified by a dimensionless factor $f_\mu$ to provide the correct asymptotic behaviour of the turbulent stresses close to a solid boundary

$$\mu_T = \bar{\rho} C_\mu f_\mu \frac{\tilde{k}^2}{\tilde{\epsilon}} \tag{2.20}$$

where asymptotic analysis (see, for example, Speziale *et al.* 1990) shows† $f_\mu = O(n^{-1})$ as $n \to 0$. Additionally, $f_\mu \to 1$ as $n \to \infty$. The dimensionless function $f_\mu$ is determined through consideration of the viscous sublayer and logarithmic region of an incompressible flat-plate turbulent boundary layer as described in the next section.

The equation for the dissipation is likewise modified by incorporation of molecular diffusion of $\tilde{\epsilon}$ in the manner proposed by Saffman (1970) and the inclusion of the dimensionless function $f_2$ for the dissipation term

$$\frac{\partial \bar{\rho}\tilde{\epsilon}}{\partial t} + \frac{\partial \bar{\rho}\tilde{u}_i\tilde{\epsilon}}{\partial x_i} = -C_{\epsilon 1}\frac{\tilde{\epsilon}}{\tilde{k}}\overline{\rho u_i'' u_j''}\frac{\partial \tilde{u}_i}{\partial x_j} - C_{\epsilon 2} f_2 \bar{\rho}\frac{\tilde{\epsilon}^2}{\tilde{k}} + \frac{\partial}{\partial x_i}\left[\left(\frac{\mu_T}{\sigma_\epsilon} + \tilde{\mu}\right)\frac{\partial \tilde{\epsilon}}{\partial x_i}\right] \tag{2.21}$$

where asymptotic analysis (Speziale *et al.* 1990) indicates $f_2 = O(n^2)$ as $n \to 0$, and $f_2 \to 1$ as $n \to \infty$.

The dimensionless function $f_2$ is taken to be

$$f_2 = 1 - \exp(-C_{\epsilon_s}\sqrt{R_t}) \tag{2.22}$$

where $R_t$ is the turbulence Reynolds number

$$R_t = \frac{\bar{\rho}\tilde{k}^2}{\tilde{\mu}\tilde{\epsilon}}. \tag{2.23}$$

This provides the proper asymptotic behaviour near the wall assuming $\epsilon \to \epsilon_w$ as

† The argument requires the assumption that the density fluctuations at the wall may be neglected. This is certainly true for incompressible flow. Although not formally correct for compressible flows (adiabatic or isothermal walls), it is nonetheless invoked (e.g. Zhang *et al.* 1992).

$n \to 0$ where $\epsilon_w$ is the (positive) value of the turbulence kinetic energy dissipation at the wall, and $\tilde{k} = O(n^2)$ as $n \to 0$. The dimensionless constant $C_{\epsilon_s}$ is determined by comparison with direct numerical simulation (DNS) results as described below.

The boundary conditions for the turbulence variables at a solid boundary are

$$\tilde{k} = 0, \quad \tilde{\epsilon} = \frac{2\tilde{\mu}_w}{\bar{\rho}_w}\left(\frac{\partial\sqrt{k}}{\partial n}\right)^2, \tag{2.24}$$

where $n$ is the normal distance to the boundary and the subscript $w$ implies evaluation at the wall. These boundary conditions are exact.

### 2.3.3. *Determination of $f_\mu$ and $C_{\epsilon_s}$*

The low Reynolds number model introduces the dimensionless functions $f_\mu$ and $f_2$. The functional form of $f_\mu$ and the constant $C_{\epsilon_s}$ in $f_2$ are determined through consideration of the viscous sublayer and logarithmic region of an incompressible flat-plate turbulent boundary layer (i.e. the 'constant stress layer') in the manner proposed by Saffman (1970). In this region, convective effects are negligible and the model equations are

$$0 = \frac{\partial}{\partial y}\left(-\overline{\rho u''v''} + \mu\frac{\partial u}{\partial y}\right), \tag{2.25}$$

$$0 = -\overline{\rho u''v''}\frac{\partial u}{\partial y} - \rho\epsilon + \frac{\partial}{\partial y}\left[\left(\frac{\mu_T}{\sigma_k} + \mu\right)\frac{\partial k}{\partial y}\right], \tag{2.26}$$

$$0 = -C_{\epsilon_1}\frac{\epsilon}{k}\overline{\rho u''v''}\frac{\partial u}{\partial y} - C_{\epsilon_2}f_2\frac{\rho\epsilon^2}{k} + \frac{\partial}{\partial y}\left[\left(\frac{\mu_T}{\sigma_\epsilon} + \mu\right)\frac{\partial\epsilon}{\partial y}\right], \tag{2.27}$$

where the Reynolds shear stress is

$$-\overline{\rho u''v''} = \mu_T\frac{\partial u}{\partial y} \tag{2.28}$$

and

$$\mu_T = \rho C_\mu f_\mu \frac{k^2}{\epsilon}. \tag{2.29}$$

The tilde is omitted since the flow is incompressible.

The boundary conditions at the wall are

$$u = 0, \tag{2.30}$$

$$k = 0, \tag{2.31}$$

$$\epsilon = \frac{2\mu}{\rho}\left(\frac{\partial\sqrt{k}}{\partial y}\right)^2, \tag{2.32}$$

and the asymptotic boundary conditions for $y \to \infty$ are

$$u = \frac{u_*}{\kappa}\ln\left(\frac{yu_*}{\nu}\right) + Bu_*, \tag{2.33}$$

$$k = \frac{u_*^2}{\sqrt{C_\mu}}, \tag{2.34}$$

$$\epsilon = \frac{u_*^3}{\kappa y}, \tag{2.35}$$

where $u_* = \sqrt{\tau_w/\rho}$ is the local friction velocity.

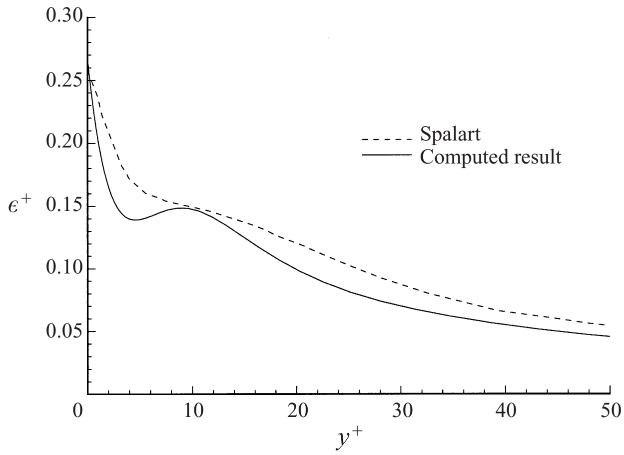


FIGURE 2. Predicted and DNS results for $\epsilon$.

For the incompressible constant-stress layer, the following form of the turbulent eddy viscosity is assumed:

$$\mu_T = \begin{cases} \rho\kappa u_* y_m[2(y/y_m)^3 - (y/y_m)^5] & \text{for } y \leqslant y_m \\ \rho\kappa u_* y & \text{for } y > y_m. \end{cases} \tag{2.36}$$

The functional form for $\mu_T$ satisfies the appropriate asymptotic forms (Wilcox 1993; Speziale *et al.* 1990) as $y \to 0$ and $y \to \infty$, and is continuously differentiable for all $y$. *It is emphasized that equation (2.36) is employed only for the incompressible constant-stress-layer analysis.*

The momentum equation (2.25) may be directly integrated, using (2.28) and (2.36) and subject to boundary conditions (2.30) and (2.33). The constant $B$ in (2.33) depends on the value of $y_m$. It may be verified that $y_m = 33.0\nu/u_*$ yields $B = 5.0$ in agreement with experiment (Monin & Yaglom 1971).

The turbulence model equations (2.26) and (2.27) may be solved for $k$ and $\epsilon$ subject to boundary conditions (2.31), (2.32), (2.34) and (2.35). The constant $C_{\epsilon_s}$ is determined by requiring $\epsilon_w = 0.26u_*^4/\nu$ in agreement with the DNS of Spalart (1988) for a flat-plate turbulent boundary layer. This yields $C_{\epsilon_s} = 0.17$. Comparison of the predicted and DNS profiles for $\epsilon$ are presented in figure 2 where $\epsilon^+ = \epsilon\nu/u_*^4$.

The dimensionless function $f_\mu$ is then obtained from (2.29) as a function of $R_t$. The functions $f_2$ and $f_\mu$ are shown in figure 3. These functions are employed without modification for the subsequent computations. The low Reynolds number modifications are summarized in table 2.

### 2.3.4. *Validation of the low Reynolds number model*

A detailed validation of the low Reynolds number model was performed for adiabatic and isothermal flat-plate zero-pressure-gradient turbulent boundary layers from incompressible to Mach 6 in Becht & Knight (1995). We present results for incompressible flow since the improvements to the model are based on arguments for incompressible turbulent flow. We also present results for Mach 4 which corresponds to the free-stream conditions for the experiments of Zheltovodov *et al.* (1994, 1998*a*, *b*) for the crossing shock, and are representative of the accuracy of the model for Mach 2 to 6 (Becht & Knight 1995).

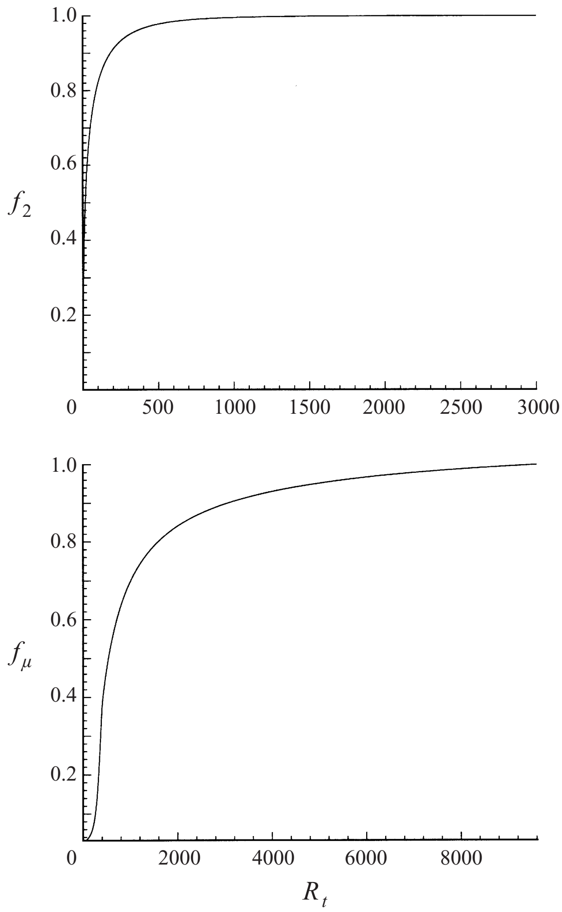


FIGURE 3. Functions $f_2$ and $f_\mu$.

| Function | Expression |
|---|---|
| $f_2(Re_t)$ | $1 - \exp(-C_{\epsilon_s}\sqrt{R_t})$ where $C_{\epsilon_s} = 0.17$ |
| $f_\mu(Re_t)$ | See figure 3 |

TABLE 2. Low Reynolds number functions.

*Incompressible flow*

The predictions of the model equations for the incompressible flat-plate boundary layer experiment of Weighardt & Tillman (1951) are presented in figures 4 and 5. The computed and experimental skin friction agree to within 9%. The velocity profiles are displayed at $Re_\theta = 1.2 \times 10^4$ and agree within 2%.

*Mach* 4 *adiabatic wall*

The computed skin friction for the adiabatic Mach 4 turbulent boundary layer is compared with the empirical Van Driest II formula (Hopkins & Inouye 1971) in

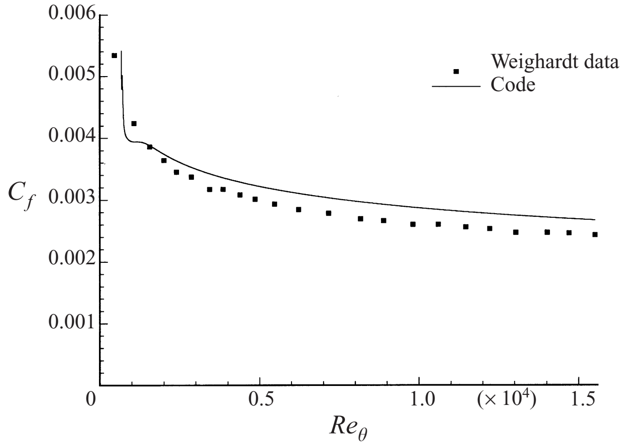


FIGURE 4. Skin friction coefficient from Weighardt & Tillman.

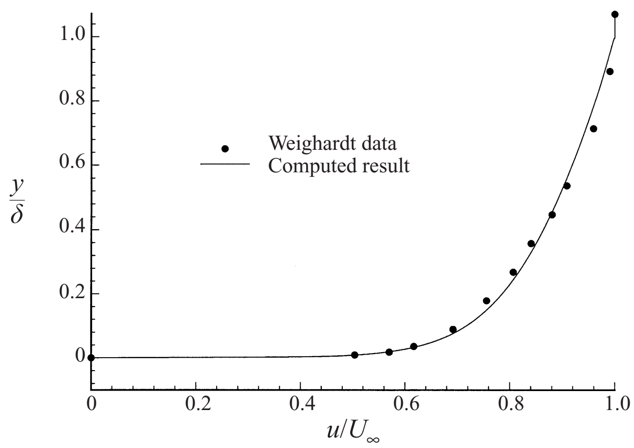


FIGURE 5. Velocity profile from Weighardt & Tillman.

figure 6. The predictions are within the experimental uncertainty ($\pm 10\%$) for the entire range of Mach numbers (Becht & Knight 1995).

The computed velocity profile in the near-wall region is presented in figure 7 and compared with the compressible law of the wall (White 1974)

$$u_c = \frac{u_*}{\kappa} \ln \frac{y u_*}{\nu_w} + \hat{B} u_* \tag{2.37}$$

where $u_c$ is the transformed compressible velocity

$$u_c = \frac{U_\infty}{A} \sin^{-1} \left\{ \frac{2A^2 v - B}{\sqrt{B^2 + 4A^2}} \right\} + \frac{U_\infty}{A} \sin^{-1} \left\{ \frac{B}{\sqrt{B^2 + 4A^2}} \right\} \tag{2.38}$$

with $v = u/U_\infty$ and $\hat{B} = 5.0$, and

$$A^2 = \frac{\gamma - 1}{2} Pr_t \frac{T_\infty}{T_w} M_\infty^2, \quad B = -\frac{Pr_t q_w U_\infty}{c_p T_w \tau_w}, \tag{2.39}$$

and $q_w$ is the heat transfer at the wall. The computed profiles demonstrate close

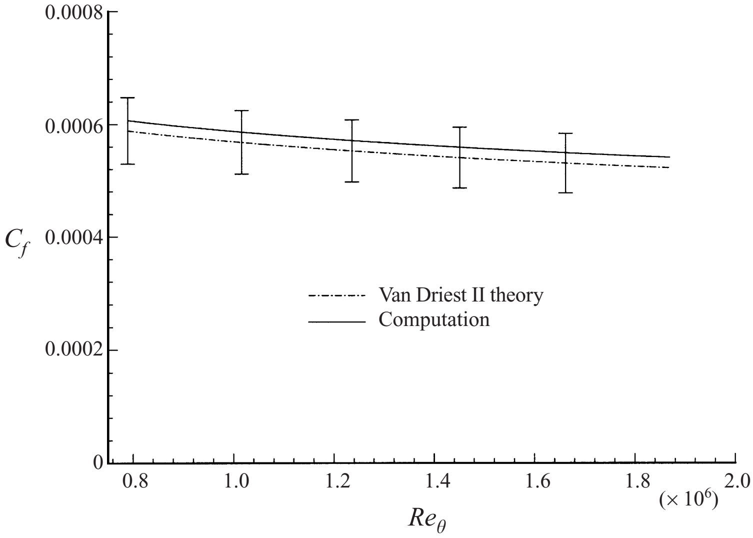


FIGURE 6. Skin friction for $M_\infty = 4$ (adiabatic).

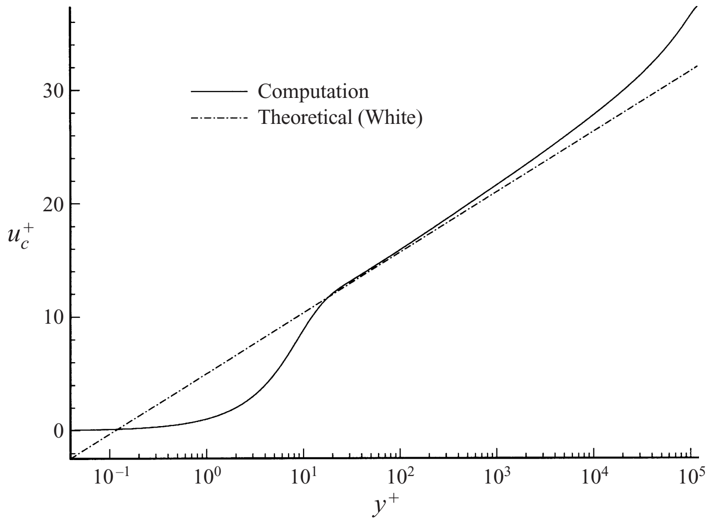


FIGURE 7. Velocity profile in the near-wall region for $M_\infty = 4$ (adiabatic).

agreement with the compressible law of the wall within a region near the wall. The computed velocity profile in the outer region is presented in figure 8 and compared with the compressible defect law (White 1974)

$$U_{e_c} - u_c = \frac{u_*}{\kappa}\left\{2\Pi\left[1 - \sin^2\left(\frac{\pi}{2}\frac{y}{\delta}\right)\right] - \ln\frac{y}{\delta}\right\} \tag{2.40}$$

where $U_{e_c}$ is the transformed compressible velocity evaluated at the edge of the boundary layer $\delta$. The defect law is a consequence of the general compressible law of the wall and wake

$$u_c = \frac{u_*}{\kappa}\ln\frac{yu_*}{\nu_w} + \hat{B}u_* + \frac{2\Pi u_*}{\kappa}\sin^2\left(\frac{\pi}{2}\frac{y}{\delta}\right) \tag{2.41}$$

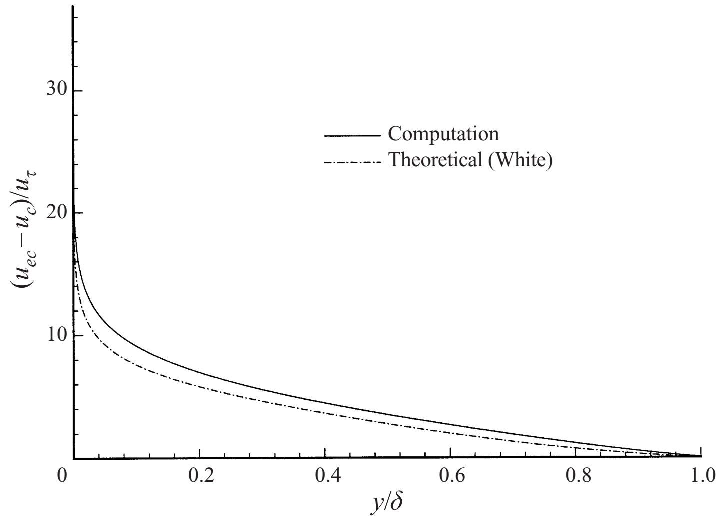


FIGURE 8. Velocity profile in the outer region for $M_\infty = 4$ (adiabatic)

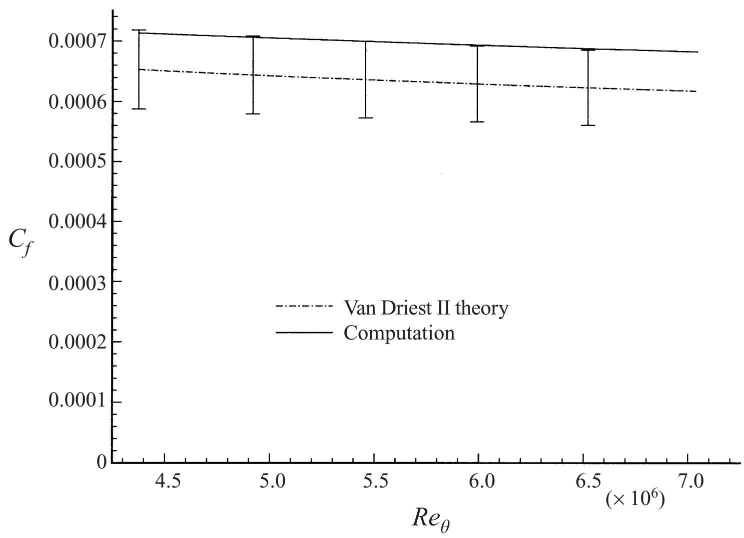


FIGURE 9. Skin friction for $M_\infty = 4$ (isothermal).

where $\Pi = 0.55$ for a flat-plate boundary layer (White 1974). The computed profile demonstrates good agreement with the defect law.

The computed adiabatic wall temperature $T_{aw}/T_\infty = 3.85$, which is within 4.7% of the value obtained from asymptotic analysis of the turbulence model equations (Knight 1993*a*)

$$T_{adia} = T_\infty \left(1 + \frac{\gamma - 1}{2}\sqrt{Pr_t} M_\infty^2\right). \tag{2.42}$$

Additionally, the computed adiabatic wall temperature agrees with the commonly used expression (White 1974), wherein $\sqrt{Pr_t}$ is replaced by $Pr_t$ in (2.42), to within 2% over the same Mach number range (Becht & Knight 1995).

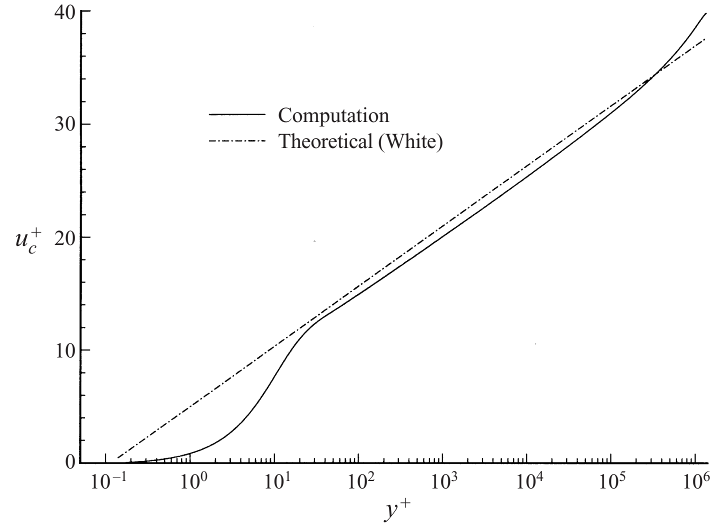


FIGURE 10. Velocity profile in the near-wall region for $M_\infty = 4$ (isothermal).

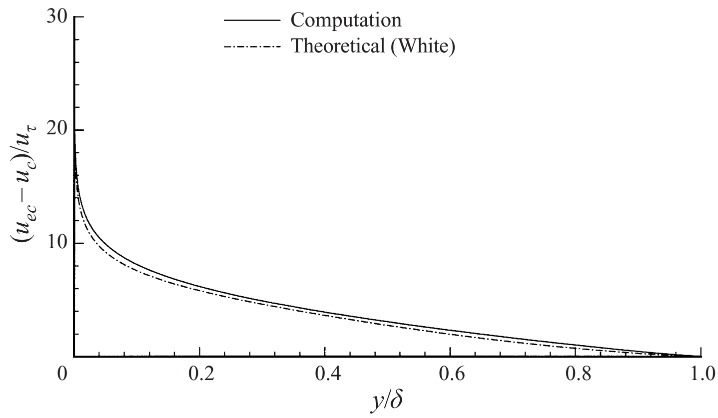


FIGURE 11. Velocity profile in the outer region for $M_\infty = 4$ (isothermal).

*Mach* 4 *isothermal wall*

The computed skin friction is compared with the empirical Van Driest II theory (Hopkins & Inouye 1971) in figure 9 for $T_w = 0.4T_{aw}$. The prediction is within the experimental uncertainty ($\pm 10\%$).

The computed Reynolds analogy factor $2C_h/C_f = 1.24$, where the heat transfer coefficient is defined as

$$C_h = \frac{q_w}{\rho_\infty U_\infty c_p (T_w - T_{adia})}. \tag{2.43}$$

This is within 12.7% of the theoretical value of 1.1 based on asymptotic analysis of the model equations (Knight 1993*a*).

The computed velocity profile in the near-wall region is presented in figure 10 and compared with the compressible law of the wall (2.37). The computed profiles demonstrate good agreement. The computed velocity profile in the outer region is presented in figure 11 and compared with the compressible defect law (2.40). Excellent agreement is observed.

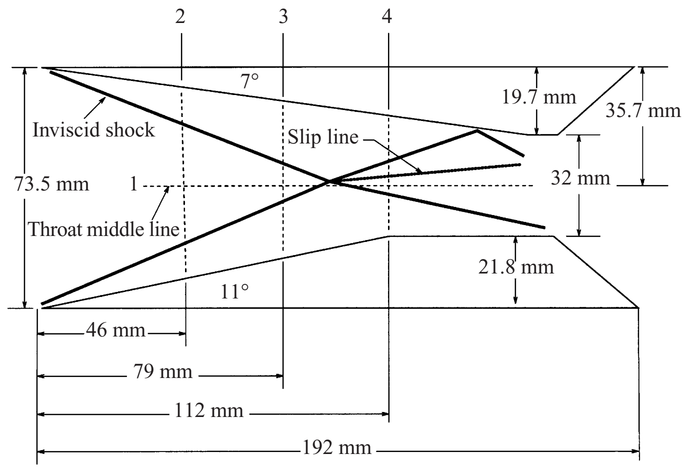


FIGURE 12. Experimental configuration for $(\alpha_1, \alpha_2) = (7^\circ, 11^\circ)$ (Zheltovodov *et al.*).

| Reference | $M_\infty$ | $\alpha_1$ | $\alpha_2$ | $Re_{\delta_\infty}$ | $p_{t_\infty}$ MPa | $T_{t_\infty}$ K | $\delta^*_\infty$ mm |
|---|---|---|---|---|---|---|---|
| Case 1 | 3.95 | 7° | 7° | $3.1 \times 10^5$ | 1.5 | 261 | 1.1 |
| Case 2 | 3.95 | 7° | 11° | $3.0 \times 10^5$ | 1.5 | 260 | 1.1 |

| | | | |
|---|---|---|---|
| $M_\infty$ | free-stream Mach number | $T_{t_\infty}$ | free-stream total temperature |
| $Re_{\delta_\infty}$ | Reynolds number based on $\delta_\infty$ | $\delta^*_\infty$ | upstream displacement thickness |
| $p_{t_\infty}$ | free-stream total pressure | $\alpha_1, \alpha_2$ | fin angles (deg) |

TABLE 3. Experimental (Zheltovodov *et al.* 1994, 1998*a*, *b*) and computational conditions.

## 3. Crossing shock interaction

### 3.1. *Details of computations*

The computational results are compared to the experimental data of Zheltovodov *et al.* (1994, 1998*a*, *b*) for the $(\alpha_1, \alpha_2) = (7^\circ, 7^\circ)$ and $(7^\circ, 11^\circ)$ configurations. For the $(\alpha_1, \alpha_2) = (7^\circ, 11^\circ)$ case, the computations are also compared with previous simulations by Knight *et al.* (1995*b*) using the low Reynolds number correction of Chien (1982), and by Zha & Knight (1996) using a full Reynolds stress equation (RSE) model. The experimental configuration, which consists of two fins mounted on a flat plate, is shown in figure 12 for $(\alpha_1, \alpha_2) = (7^\circ, 11^\circ)$. The incoming flow parameters are summarized in table 3.

The inflow profiles were generated with a boundary layer code (Becht & Knight 1995) which utilizes the same turbulence model. The inflow profile matches the experimental displacement thickness. The thin boundary layers on sidewalls can be neglected since the reflected shock waves either intersect the sidewalls near the exit or not at all (Knight *et al.* 1995*b*; Zha & Knight 1996).

The CRAFT code (Molvik & Merkle 1989), modified to incorporate the low Reynolds number model of Becht & Knight, was used for all computations. The code solves the full three-dimensional Reynolds-averaged compressible Navier–Stokes equations coupled with the turbulence model equations. The code utilizes the method of Roe (1981) for the inviscid fluxes, central differencing for the viscous fluxes and turbulence

| Reference | $\alpha_1$ (deg.) | $\alpha_2$ (deg.) | Wall | $N_x$ | $N_y$ | $N_z$ |
|---|---|---|---|---|---|---|
| Case 1a | 7 | 7 | I | 101 | 79 | 49 |
| Case 1b | 7 | 7 | A | 101 | 79 | 49 |
| Case 2a | 7 | 11 | I | 101 | 81 | 49 |
| Case 2b | 7 | 11 | A | 101 | 81 | 49 |
| Case 2c | 7 | 11 | I | 202 | 81 | 49 |
| Case 2d | 7 | 11 | I | 101 | 162 | 49 |
| Case 2e | 7 | 11 | I | 101 | 81 | 98 |
| Case 2f | 7 | 11 | I | 101 | 81 | 49 |

| Reference | $\Delta x/\delta_\infty$ | $\Delta y_{min}/\delta_\infty$ | $\Delta y_{max}/\delta_\infty$ | $\Delta z_{min}/\delta_\infty$ | $\Delta z_{max}/\delta_\infty$ | $\Delta y_2^+\vert_{rms}$ | $\Delta y_2^+\vert_{aver}$ |
|---|---|---|---|---|---|---|---|
| Case 1a | 0.5 | $2.2 \times 10^{-4}$ | 0.5 | 0.2 | 0.5 | 0.55 | 0.52 |
| Case 1b | 0.5 | $2.2 \times 10^{-4}$ | 0.5 | 0.2 | 0.5 | 0.63 | 0.59 |
| Case 2a | 0.5 | $2.2 \times 10^{-4}$ | 0.5 | 0.2 | 0.5 | 0.70 | 0.62 |
| Case 2b | 0.5 | $2.2 \times 10^{-4}$ | 0.5 | 0.2 | 0.5 | 0.80 | 0.72 |
| Case 2c | 0.25 | $2.2 \times 10^{-4}$ | 0.5 | 0.2 | 0.5 | 0.72 | 0.65 |
| Case 2d | 0.5 | $1.1 \times 10^{-4}$ | 0.25 | 0.2 | 0.5 | 0.35 | 0.31 |
| Case 2e | 0.5 | $2.2 \times 10^{-4}$ | 0.5 | 0.1 | 0.25 | 0.70 | 0.63 |
| Case 2f | 0.5 | $2.2 \times 10^{-4}$ | 0.5 | 0.2 | 0.5 | 0.68 | 0.60 |

LEGEND

| | | | |
|---|---|---|---|
| $N_x$ | number of points in $x$ | I | Isothermal wall |
| $N_y$ | number of points in $y$ | A | Adiabatic wall |
| $N_z$ | number of points in $z$ | | |
| $\Delta y_2^+\vert_{rms}$ | r.m.s. grid spacing at wall in wall units | | |
| $\Delta y_2^+\vert_{aver}$ | average grid spacing at wall in wall units | | |

TABLE 4. Details of computations.

source terms and an approximate factorization of the Jacobian. The modified CRAFT code was validated through comparison of results for adiabatic and isothermal flat-plate compressible turbulent boundary layers with separate computations performed with a boundary layer code (Becht 1994) incorporating the same turbulence model.

For each configuration, two separate computations were performed in order to determine the local heat transfer coefficient (2.43). First, the wall temperature was fixed at $T_w = 1.031 T_{t_\infty}$, and the local heat transfer $q_w(x, z)$ determined. Then, the wall was assumed adiabatic and the local adiabatic wall temperature $T_{aw}(x, z)$ was determined. This approach has been employed previously for comparison with experimental heat transfer (Knight *et al.* 1995*b*; Zha & Knight 1996; Lee, Settles & Horstman 1992).

Details of the computational grids are presented in table 4. For each case, the isothermal and adiabatic computations are indicated (e.g. Case 1a and 1b). For the $(\alpha_1, \alpha_2) = (7°, 11°)$ configuration, four additional computations were performed. Three of these computations (Cases 2c to 2e) represent a grid refinement study wherein the number of grid points in each direction was successively doubled. The fourth additional computation (Case 2f) incorporated a different wall temperature ($T_w = 1.0385 T_{t_\infty}$). The results of the four additional computations showed no significant change in the predictions of the bottom surface flow pattern, pressure, adiabatic wall temperature and heat transfer predictions within the region of comparison with experiment (Gnedin 1996). Therefore, the $(\alpha_1, \alpha_2) = (7°, 11°)$ computation represents an effectively grid-converged solution. Since the grid employed for the

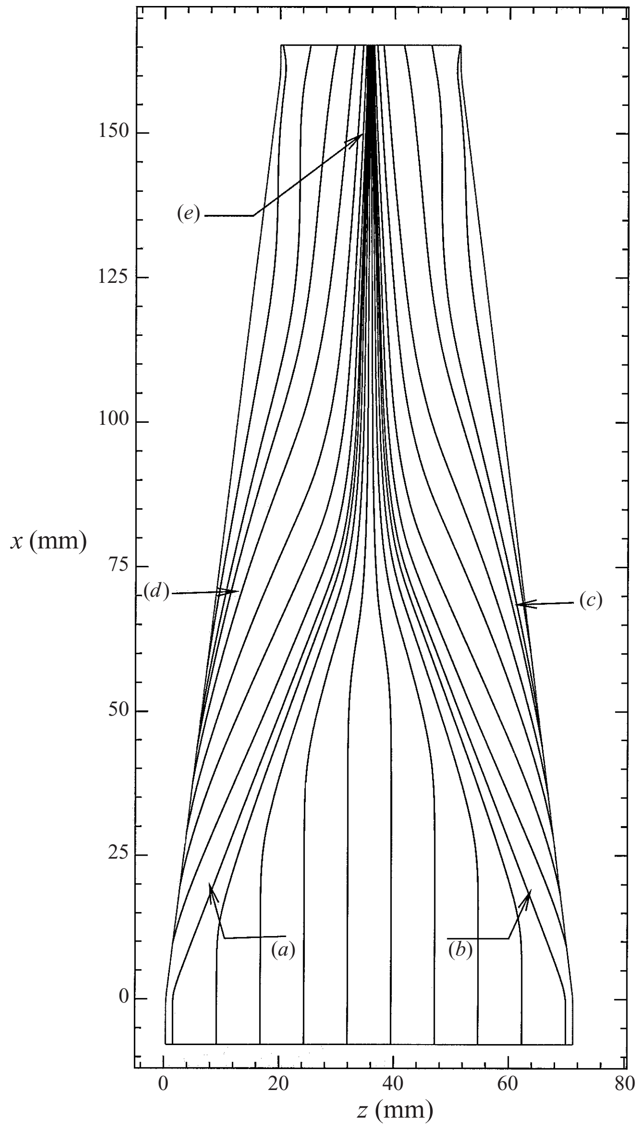


FIGURE 13. Computed skin friction lines for $(\alpha_1, \alpha_2) = (7°, 7°)$: (*a*) left incident separation line; (*b*) right incident separation line; (*c, d*) lines of divergence; (*e*) downstream coalescence line.

weaker $(\alpha_1, \alpha_2) = (7°, 7°)$ case was essentially the same as used for $(\alpha_1, \alpha_2) = (7°, 11°)$, we therefore consider the $(\alpha_1, \alpha_2) = (7°, 7°)$ computation to be grid-converged also.

### 3.2. *Results for* $(\alpha_1, \alpha_2) = (7°, 7°)$

The computed surface skin friction lines and experimental surface flow visualization for the $(\alpha_1, \alpha_2) = (7°, 7°)$ configuration are presented in figures 13 and 14, respectively. The separation lines (lines of coalescence) (*a*) and (*b*) originating from the fin leading edges are apparent in the computation and experiment. The computed and experimental separation line angles agree within 7%. The computed skin friction lines do not intersect but, after changing direction, slowly converge towards each other. Two weak divergence lines (*c*) and (*d*) can be found near the fin surfaces.

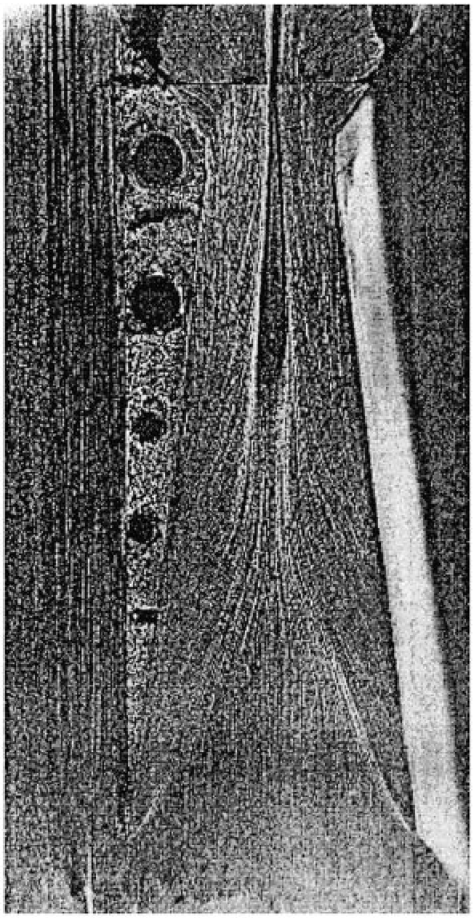

FIGURE 14. Experimental surface flow for $(\alpha_1, \alpha_2) = (7°, 7°)$.

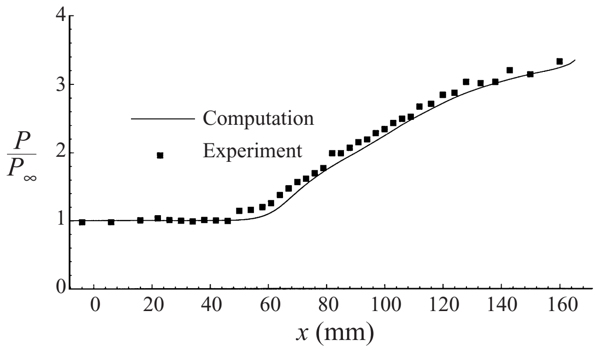


FIGURE 15. Wall pressure on TML for $(\alpha_1, \alpha_2) = (7°, 7°)$.

The computed and experimental surface pressure, normalized by the free-stream static pressure $p_\infty$, are displayed in figures 15 and 16 along the throat middle line (TML) (the streamwise line which bisects the channel at its minimum cross section) and at the three streamwise locations. The uncertainty in the surface pressure

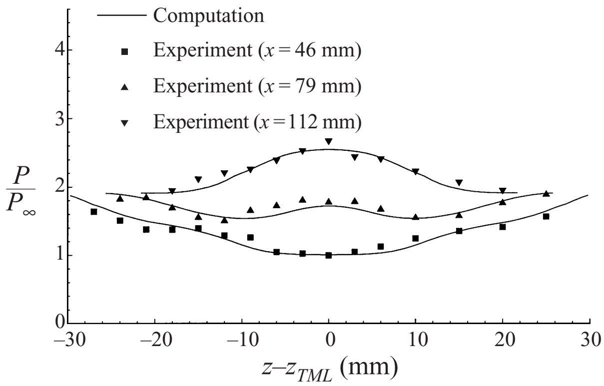


FIGURE 16. Wall pressure at $x = 46$ mm, $x = 79$ mm and $x = 112$ mm for $(\alpha_1, \alpha_2) = (7°, 7°)$.

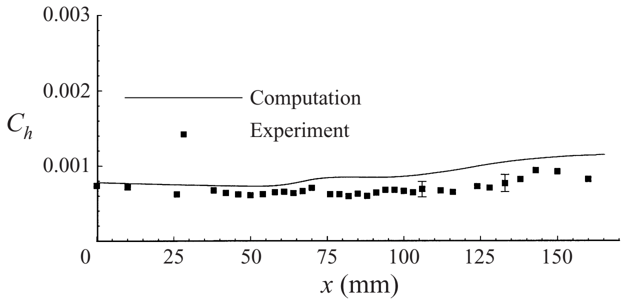


FIGURE 17. $C_h$ on TML for $(\alpha_1, \alpha_2) = (7°, 7°)$.

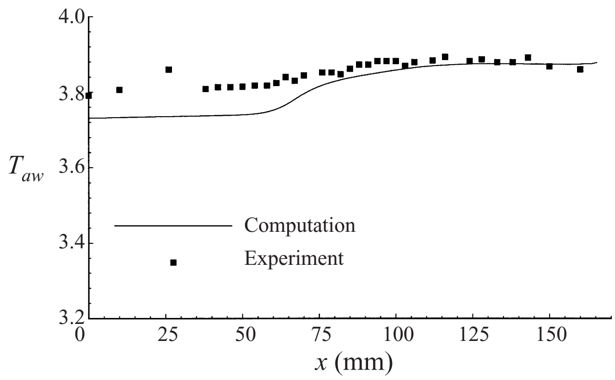


FIGURE 18. $T_{aw}$ on TML for $(\alpha_1, \alpha_2) = (7°, 7°)$.

measurements is $\pm 0.5\%$. The computed surface pressure displays excellent agreement with experiment.

The computed and experimental surface heat transfer coefficient $C_h$ on the TML is presented in figure 17. The experimental uncertainty for $C_h$ is $\pm 10\%$ to $\pm 15\%$. Reasonable agreement with the experiment is observed. The heat transfer coefficient is predicted typically within 25% in the three-dimensional interaction region. The slight increase in $C_h$ within the three-dimensional interaction is also predicted.

The adiabatic wall temperature $T_{aw}$ on the TML is presented in figure 18. The

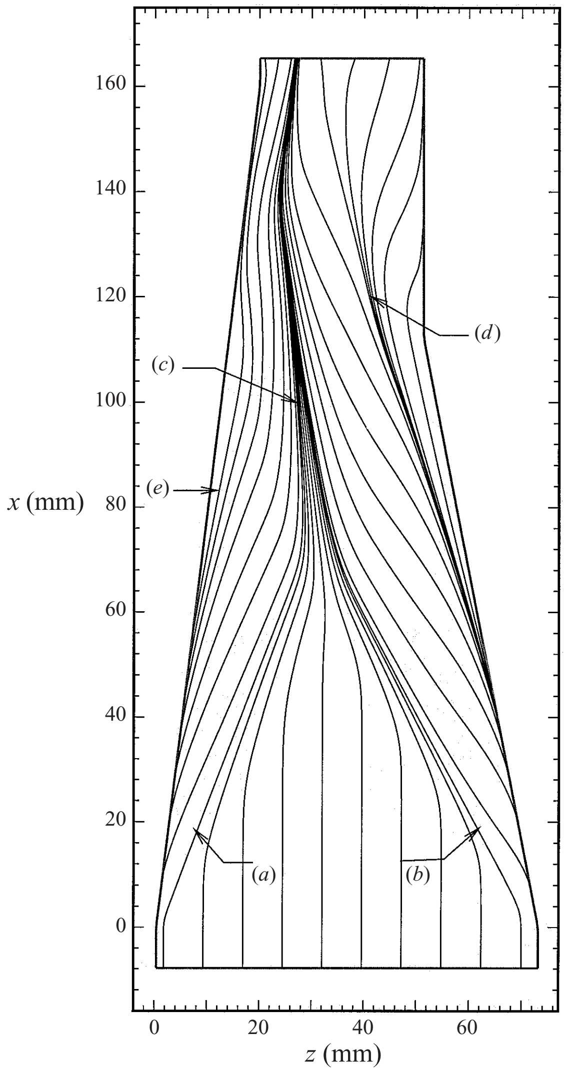


FIGURE 19. Computed skin friction lines for $(\alpha_1, \alpha_2) = (7^\circ, 11^\circ)$: (*a*) left incident separation line; (*b*) right incident separation line; (*c*) left downstream coalescence line; (*d, e*) lines of divergence.

experimental uncertainty in $T_{aw}$ is less than 0.2%. Close agreement is observed. The maximum difference between the predicted and measured $T_{aw}$ is less than 2%.

### 3.3. *Results for* $(\alpha_1, \alpha_2) = (7^\circ, 11^\circ)$

Figures 19 and 20 present the computed surface skin friction lines and experimental surface flow visualization respectively. It has been previously noted (Knight *et al.* 1995*b*; Narayanswami, Horstman & Knight 1993*b*) that the computed surface skin friction lines are sensitive to the turbulence model employed. Comparison of current results with figure 6 of Knight *et al.* (1995*b*) shows general agreement as well as a number of substantially different details. Both incident separation lines emanating from the fin leading edges (*a* and *b*) are clearly observed in figure 19 in agreement with experimental results and previous simulations of Knight *et al.* (1995*b*). These separation lines are associated with the incident single-fin interactions. The computed

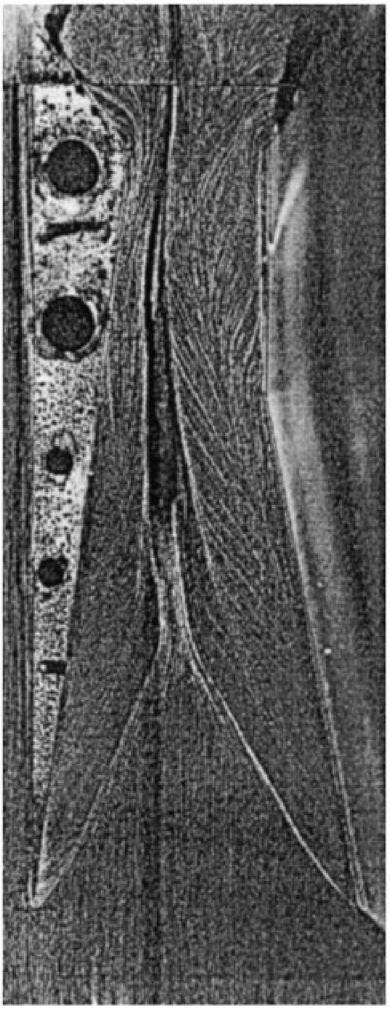

FIGURE 20. Experimental surface flow for $(\alpha_1, \alpha_2) = (7^\circ, 11^\circ)$.

and experimental separation line angles, measured relative to the $x$-axis, agree within 9%. However, contrary to the computation with the $k$–$\epsilon$ Chien model (Knight *et al.* 1995*b*), the incident separation lines do not coalesce near the centre of the region, but rather continue further downstream almost in parallel until they converge at $x \approx 110$ mm to form a narrow band of skin friction lines (*c*), which is offset to the left-hand side of the channel. This is denoted in Knight *et al.* (1995*b*) as the left downstream coalescence line, and represents the surface image of the boundary between the left- and right-hand vortices generated by the incident single-fin interactions. The vortices are evident in the crossflow velocity vectors (figure 21) at $x = 112$ mm. The crossflow velocity vectors near the surface change direction at (*c*). Lines of divergence are also apparent near the right-hand fin (*d*) and left-hand fin (*e*) associated with the incident single-fin interaction. In a major difference with the $k$–$\epsilon$ Chien model results, a second line of coalescence (the right downstream coalescence line) is not present in this computation. Consequently, the model does not predict a secondary separation underneath the left-hand side of the right-hand vortex (see Knight *et al.* 1995*b*). The

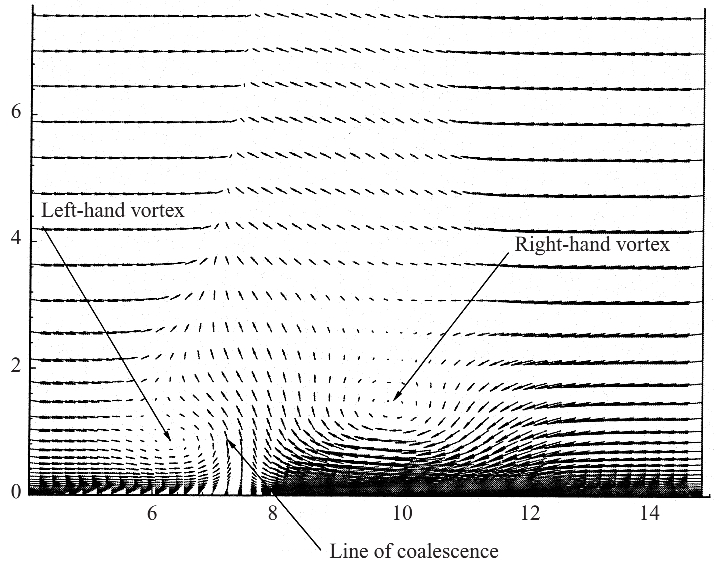


FIGURE 21. Crossflow velocity vectors at $x = 112\,\mathrm{mm}$ for $(\alpha_1, \alpha_2) = (7°, 11°)$.

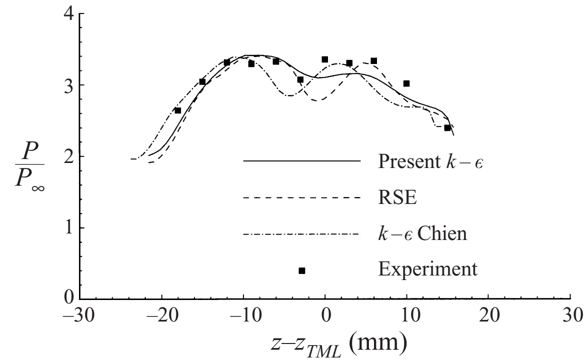


FIGURE 22. Wall pressure at $x = 112\,\mathrm{mm}$ for $(\alpha_1, \alpha_2) = (7°, 11°)$.

difference is due to deviation in the predictions of the pressure distribution in the spanwise direction, obtained with each turbulence model as described below.

The computed and experimental surface pressure distribution in the spanwise direction at $x = 112\,\mathrm{mm}$, normalized by the free-stream static pressure $p_\infty$, is displayed in figure 22. This location corresponds to the streamwise location No. 4 (see figure 12). The plot contains computational results obtained with three different turbulence models as described above. The abscissa $z–z_{\mathrm{TML}}$ represents the spanwise distance measured from the TML. The computed and experimental surface pressure are in general agreement for all three models. However, unlike in the present computations, Chien's model predicts a local adverse pressure gradient in spanwise direction in the region $-10\,\mathrm{mm} < z–z_{\mathrm{TML}} < -4\,\mathrm{mm}$. As described in detail in Knight *et al.* (1995*b*), the flow near the surface at this location is moving towards the left-hand fin and the adverse pressure gradient causes the secondary separation and the appearance of the right downstream coalescence line, which is not predicted by the present computation.

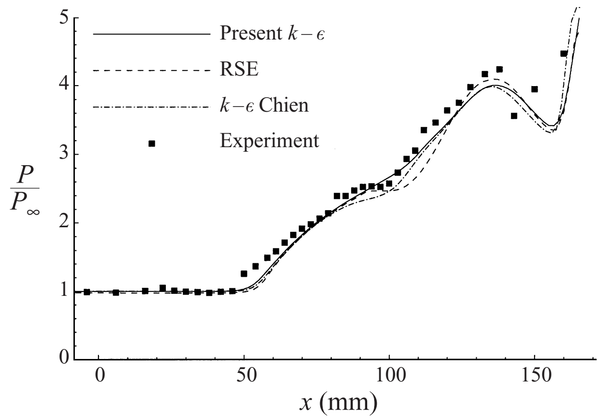


FIGURE 23. Wall pressure on TML for $(\alpha_1, \alpha_2) = (7°, 11°)$.

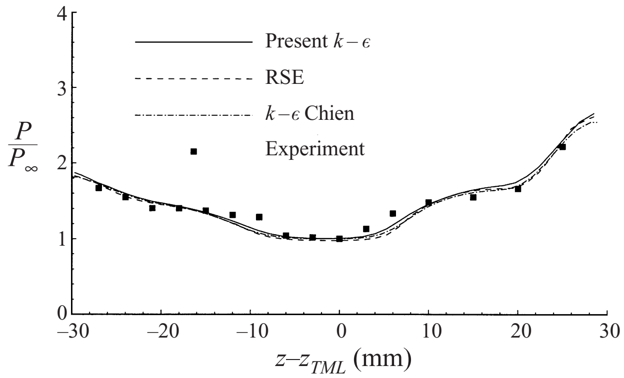


FIGURE 24. Wall pressure at $x = 46$ mm for $(\alpha_1, \alpha_2) = (7°, 11°)$.

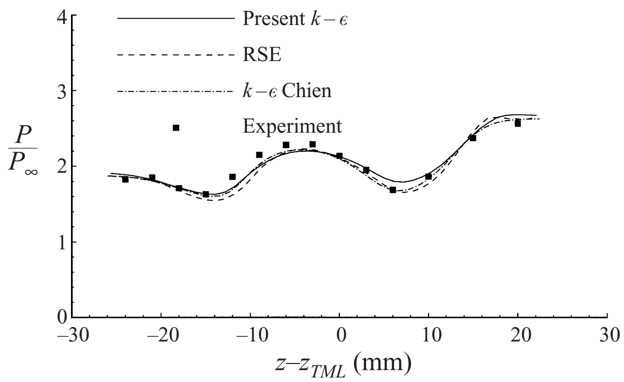


FIGURE 25. Wall pressure at $x = 79$ mm for $(\alpha_1, \alpha_2) = (7°, 11°)$.

The computed and experimental surface pressure along the TML, displayed in figure 23, are in good agreement for $x < 135$ mm, although the computation underestimates the extent of the upstream influence, as observed in previous studies (e.g. Narayanswami *et al.* 1992; Knight *et al.* 1995*b*). The computed pressure does not

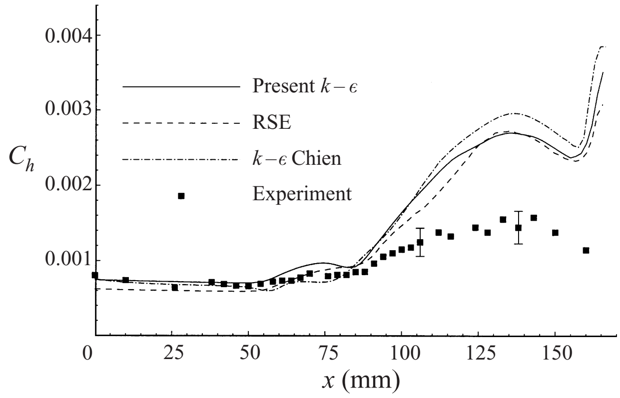


FIGURE 26. $C_h$ on TML for $(\alpha_1, \alpha_2) = (7^\circ, 11^\circ)$.

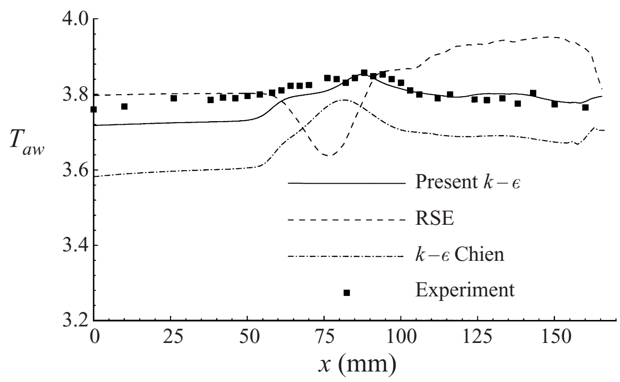


FIGURE 27. $T_{aw}$ on TML for $(\alpha_1, \alpha_2) = (7^\circ, 11^\circ)$.

accurately predict the pressure rise (beginning at $x = 145$ mm) associated with the shock reflection from the 7° fin, since all of the computations omit the boundary layers on the fin surfaces. The computed and experimental surface pressure at $x = 46$ and 79 mm are displayed in figures 24 and 25. Close agreement is again observed.

The computed and experimental surface heat transfer coefficient $C_h$ on the TML is presented in figure 26. All three turbulence models overpredict the heat transfer by approximately a factor of two downstream of the intersection of the shocks (which occurs at $x = 93.7$ mm), with a modest improvement in the computations performed with RSE and present models compared to the $k$–$\epsilon$ Chien model. The overprediction in $C_h$ is actually an overprediction in $q_w$, since a series of studies (Zha & Knight 1996; Gnedin 1996) has demonstrated that the computed $q_w$ is proportional to the computed $T_w - T_{aw}$. A possible explanation is that the turbulence models overestimate the effects of the shock/boundary layer interaction on the turbulence production, thereby generating excessive turbulence kinetic energy and overestimating the turbulent thermal conductivity. Further experiments (in particular, measurements of the turbulence statistics within the flowfield) are needed to assist in the identification of the specific weaknesses in these models and develop improved models.

The computed and experimental $T_{aw}$ on the TML are displayed in figures 27 and 28. The results of the present computation exhibit excellent agreement with the experiment, and represent an improvement over the predictions by the $k$–$\epsilon$ Chien and

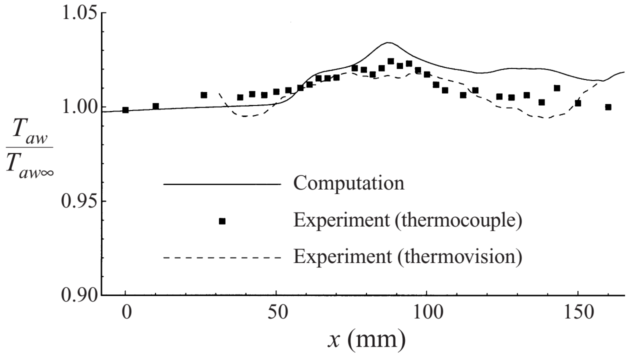


FIGURE 28. $T_{aw}$ on TML for $(\alpha_1, \alpha_2) = (7°, 11°)$.

RSE (Zha & Knight) models. The experimental results for $T_{aw}$ obtained using the thermocouple and thermovision techniques agree closely, with a maximum difference of 1.5%.

## 4. Conclusions

A collaborative experimental and theoretical (computational) study of a crossing-shock-wave/turbulent-boundary-layer interaction has been performed. Two configurations – $(\alpha_1, \alpha_2) = (7°, 7°)$ and $(7°, 11°)$ – have been examined at Mach 3.9. Experimental data include surface pressure and heat transfer, adiabatic wall temperature and surface flow visualization. The computations employ the three-dimensional Reynolds-averaged compressible Navier–Stokes equations. Turbulence is represented by the two-equation $k$–$\epsilon$ model with a new low-Reynolds-number model which has been validated for compressible adiabatic and isothermal flat-plate zero-pressure-gradient boundary layers. For the $(\alpha_1, \alpha_2) = (7°, 11°)$ configuration, previous results obtained using the $k$–$\epsilon$ Chien model and a full Reynolds stress equation (Zha & Knight) model are also presented for comparison. The principal conclusions are:

The computed surface pressure displays very good agreement with experiment for the $(\alpha_1, \alpha_2) = (7°, 7°)$ and $(7°, 11°)$ configurations. For the $(7°, 11°)$ case, similar very good agreement is obtained by the $k$–$\epsilon$ Chien and full RSE models.

The computed surface skin friction lines are in close agreement with experiment for the initial separation lines, and are in qualitative agreement within the crossing shock interaction region. However, for the $(\alpha_1, \alpha_2) = (7°, 11°)$ case, the present model does not predict the secondary separation line. This feature is predicted by the $k$–$\epsilon$ Chien model.

The computed heat transfer is in good agreement with experimental data for the $(\alpha_1, \alpha_2) = (7°, 7°)$ configuration. For the $(\alpha_1, \alpha_2) = (7°, 11°)$ configuration, the computed heat transfer is significantly overpredicted within the three-dimensional interaction. However, a modest improvement is achieved compared to the computations with the $k$–$\epsilon$ Chien model, and the results are comparable with the predictions of the full RSE model.

The adiabatic wall temperature is accurately predicted for all configurations. For the $(\alpha_1, \alpha_2) = (7°, 11°)$ case, the model displays a definite improvement over the $k$–$\epsilon$ Chien and full RSE models.

The experimental data for $T_{aw}$ obtained with the thermocouple and thermovision techniques are in close agreement.

Additional experimental data, including turbulence measurements within the three-dimensional interaction, are needed to improve the understanding of the flow field and assist in the development of improved models.

New turbulence models are needed to improve prediction of flow-field quantities of engineering interest (e.g. surface heat transfer) which are strongly influenced by the turbulence structure.

This research was sponsored by the Air Force Office of Scientific Research under grant F49620-93-1-0005 (monitored by Dr Len Sakell), NASA Ames Research Center under Grant NAG 2-798 (monitored by Drs C. C. Horstman and Tom Coakley), the Advanced Research Projects Agency under contract DABT-63-93-C-0064 (monitored by Dr Bob Lucas), and by the Russian Foundation for Basic Research under project codes 96-01-01777 and 97-01-00885. The computations were performed at the DoD Shared Resource Center at the Naval Oceanographic Office (Stennis Space Center) and at the DoD High Performance Computing Center (USAE Waterways Experiment Station). Postprocessing was performed at the Rutgers College of Engineering Supercomputer Remote Access Center. The authors express appreciation to Sanford Dash, Robert Lee, Neeraj Sinha, and Brian York for the use of the CRAFT code, and to Drs A. Maksimov, A. Shevchenko and S. Vorontsov for their collaboration on previous stages of the studies.

## REFERENCES

Becht, R. 1994 Evaluation of a low Reynolds number correction to the $k-\epsilon$ two equation compressible turbulence model. Master's thesis, Rutgers University, Dept Mechanical and Aerospace Engineering.

Becht, R. & Knight, D. 1995 A simple low Reynolds number modification for the compressible $k$–$\epsilon$ model. *AIAA Paper* 95-1111.

Chien, K.-Y. 1982 Predictions of channel and boundary layer flows with a low Reynolds number turbulence model. *AIAA J.* **20**, 33–38.

Degrez, G. (Ed.) 1993 *AGARD Special Course on Shock-Wave/Turbulent Boundary-Layer Interactions in Supersonic and Hypersonic Flow*. AGARD Rep. 792.

Dutoya, D. & Michard, P. 1981 A program for calculating boundary layers along compressor and turbine blades. In *Numerical Methods in Heat Transfer* (ed. R. Lewis, K. Morgan & O. Zienkiewicz). John Wiley and Sons.

Edwards, C. 1976 A forebody design technique for highly integrated bottom-mounted scramjets with application to a hypersonic research airplane. *Tech. Rep.* TN D-8369. NASA.

Fan, S., Lakshminarayana, B. & Barnett, M. 1993 Low Reynolds number $k$–$\epsilon$ model for unsteady turbulent boundary layer flows. *AIAA J.* **31**, 1777–1784.

Gaitonde, D. & Shang, J. 1995 Structure of a turbulent double-fin interaction at Mach 4. *AIAA J.* **33**, 2250–2258.

Gaitonde, D., Shang, J., Garrison, T., Zheltovodov, A. & Maksimov, A. 1997 Evolution of the separated flowfield in a 3-D shock wave turbulent boundary layer interaction. *AIAA Paper* 97-1837.

Gaitonde, D., Shang, J. & Visbal, M. 1995 Structure of a double-fin turbulent interaction at high speed. *AIAA J.* **33**, 193–200.

Gaitonde, D., Visbal, M., Shang, J., Zheltovodov, A. & Maksimov, A. 1998 Parametric investigation of flowfield structure and validation issues in 3-D crossing shock wave/turbulent boundary layer interactions. In *Proc. Intl Conf. on Methods of Aerophysical Research*, pp. 67–76. Russian Academy of Sciences, Siberian Division.

Garrison, T. 1994 The interaction between crossing-shock waves and a turbulent boundary layer. PhD thesis, Penn State University.

Garrison, T. & Settles, G. 1992 Flowfield visualization of crossing shock-wave/boundary layer interactions. *AIAA Paper* 92-0750.

Garrison, T. & Settles, G. 1993 Interaction strength and model geometry effects on the structure of crossing-shock wave/turbulent boundary-layer interactions. *AIAA Paper* 93-0780.

Garrison, T., Settles, G., Narayanswami, N. & Knight, D. 1992 Structure of crossing-shock wave/turbulent boundary layer interactions. *AIAA Paper* 92-3670.

Garrison, T., Settles, G., Narayanswami, N. & Knight, D. 1994 Comparison of flowfield surveys and computations of a crossing-shock wave/boundary-layer interaction. *AIAA Paper* 94-2273.

Gnedin, M. 1996 Numerical Simulation of 3-D shock wave turbulent boundary layer interaction using a two equation model of turbulence. PhD thesis, Rutgers University.

Greene, J. 1970 Interactions between shock waves and turbulent boundary layers. In *Progress in Aerospace Science*, vol. 11, pp. 235–340. Pergamon.

Hassid, S. & Poreh, M. 1978 A turbulent energy dissipation model for flows with drag reduction. *Trans ASME*: *J. Fluids Engng* **100**, 107–112.

Hoffman, G. 1975 Improved form of the low Reynolds number $k$–$\epsilon$ turbulence model. *Phys. Fluids* **18**, 309–312.

Hopkins, E. & Inouye, M. 1971 An evaluation of theories for predicting turbulent skin friction and heat transfer on flat plates at supersonic and hypersonic Mach numbers. *AIAA J.* **9**, 993–1003.

Jones, W. & Launder, B. 1972 The prediction of laminarization with a two equation model of turbulence. *Intl J. Heat Mass Transfer* **15**, 301–304.

Jones, W. & Launder, B. 1973 The calculation of low-Reynolds-number phenomena with a two-equation model of turbulence. *Intl J. Heat Mass Transfer* **16**, 1119–1130.

Knight, D. 1993*a* Compressible wall layer for $k$–$\epsilon$ model. *Internal Rep.* B-4. Dept of Mech. and Aero. Engng, Rutgers University.

Knight, D. 1993*b* Numerical simulations of 3-D shock wave turbulent boundary layer interactions. AGARD FDP/VKI Special Course on Shock Wave/Boundary Layer Interactions.

Knight, D., Garrison, T., Settles, G., Zheltovodov, A., Maksimov, A., Shevchenko, A. & Vorontsov, S. 1995*a* Asymmetric crossing shock wave/turbulent boundary layer interaction. *AIAA J.* **33**, 2241–2249.

Knight, D., Garrison, T., Settles, G., Zheltovodov, A., Maksimov, A., Shevchenko, A. & Vorontsov, S. 1995*b* Asymmetric crossing shock wave-turbulent boundary layer interaction. *AIAA Paper* 95-0231.

Lam, C. & Bremhorst, K. 1981 Modified form of the $k$–$\epsilon$ model for predicting wall turbulence. *Trans. ASME*: *J. Fluids Engng* **103**, 456–460.

Launder, B. & Sharma, B. 1974 Application of the energy dissipation model of turbulence to the calculation of flow near a spinning disk. *Lett. Heat Mass Transfer* **1**, 131–138.

Lee, Y., Settles, G. & Horstman, C. 1992 Heat transfer measurements and CFD comparison of swept shock wave/boundary layer interactions. *AIAA Paper* 92-3665.

Molvik, G. & Merkle, C. 1989 A set of strongly coupled, upwind algorithms for computing flows in chemical nonequilibrium. *AIAA Paper* 89-0199.

Monin, A. & Yaglom, A. 1971 *Statistical Fluid Mechanics: Mechanics of Turbulence*. The MIT Press.

Myong, H. & Kasagi, N. 1990 A new approach to the improvement of $k$–$\epsilon$ turbulence model for wall-bounded shear flows. *JSME Intl J.* **33**, 63–72.

Narayanswami, N., Horstman, C. C. & Knight, D. 1993*a* Computation of crossing shock turbulent boundary layer interaction at Mach 8.3. *AIAA J.* **31**, 1369–1376.

Narayanswami, N., Horstman, C. C. & Knight, D. 1993*b* Numerical simulation of crossing shock/turbulent boundary layer interaction at Mach 8.3 – comparison of zero- and two-equation turbulence models. *AIAA Paper* 93-0779.

Narayanswami, N., Knight, D., Bogdonoff, S. & Horstman, C. 1992 Interaction between crossing oblique shocks and a turbulent boundary layer. *AIAA J.* **30**, 1945–1952.

Narayanswami, N., Knight, D. & Horstman, C. C. 1993*c* Investigation of a hypersonic crossing shock wave/turbulent boundary layer interaction. *Shock Waves* **3**, 35–48.

Patel, V., Rodi, W. & Scheuerer, G. 1985 Turbulence modelling for nearwall and low Reynolds number flows: A review. *AIAA J.* **23**, 1308–1319.

Reynolds, W. 1976 Computation of turbulent flows. *Ann. Rev Fluid Mech.* **8**, 183–208.

Roe, P. 1981 Approximate Riemann solvers, parameter vectors, and difference schemes. *J. Comput. Phys.* **43**, 357–372.

Saffman, P. 1970 A model for inhomogeneous turbulent flow. *Proc. R. Soc. Lond.* A **317**, 417–433.

Sakell, L., Knight, D. & Zheltovodov, A. (Eds.) 1994 *Proc. AFOSR Workshop on Fluid Dynamics of High Speed Inlets*. Department of Mechanical and Aerospace Engineering, Rutgers University, New Brunswick, NJ.

Settles, G. & Dolling, D. 1986 Swept shock wave boundary layer interactions. In *Tactical Missile Aerodynamics*, pp. 297–379. AIAA.

Settles, G. & Dolling, D. 1990 Swept shock/boundary-layer interactions – tutorial and update. *AIAA Paper* 90-0375.

So, R., Zhang, H. & Speziale, C. 1991 Near-wall modelling of the dissipation rate equation. *AIAA J.* **29**, 2069–2076.

Spalart, P. 1988 Direct simulation of a turbulent boundary layer up to $Re_\theta = 1410$. *J. Fluid Mech.* **187**, 61–98.

Speziale, C., Abid, R. & Anderson, E. C. 1990 A critical evaluation of two-equation models for near wall turbulence. *AIAA Paper* 90-1481.

Weighardt, K. & Tillman, W. 1951 On the turbulent friction layer for rising pressure. *Tech. Rep.* TM 1314. NACA.

White, F. 1974 *Viscous Fluid Flow*. McGraw Hill.

Wilcox, D. C. 1993 *Turbulence Modelling for CFD*. DCW Industries.

Yang, Z. & Shih, T. 1993 A Galilean and tensorial invariant $k - \epsilon$ model for near wall turbulence. *AIAA Paper* 93-3105.

Zha, G.-C. & Knight, D. 1996 Three-dimensional shock/boundary layer interaction using Reynolds stress equation turbulence model. *AIAA J.* **34**, 1313–1320.

Zhang, H., So, R., Speziale, C. & Lai, Y. 1992 A near-wall two-equation model for compressible turbulent flows. *AIAA Paper* 92-0442.

Zheltovodov, A. 1996 Shock waves/turbulent boundary layer interactions: fundamental studies and applications. *AIAA Paper* 96-1977.

Zheltovodov, A., Maksimov, A. & Shevchenko, A. 1998*a* Topology of three dimensional separation under the conditions of symmetrical interaction of crossing shocks and expansion waves with turbulent boundary layer. *Thermophys. Aeromech.* **5** (3), 293–312.

Zheltovodov, A., Maksimov, A., Shevchenko, A. & Knight, D. 1998*b* Topology of three dimensional separation under the conditions of asymmetrical interaction of crossing shocks and expansion waves with turbulent boundary layer. *Thermophys. Aeromech.* **5** (4), 483–503.

Zheltovodov, A., Maksimov, A., Shevchenko, A., Vorontsov, S. & Knight, D. 1994 Experimental study and computational comparison of crossing shock wave-turbulent boundary layer interaction. In *Proc. Intl Conf. on Methods of Aerophysical Research*, pp. 221–230. Russian Academy of Sciences, Siberian Division.